

Journal of Geophysical Research: Oceans

RESEARCH ARTICLE

10.1029/2017JC013739

Key Points:

- Demonstrating the existence of the SPB in the IOD predictions
- Identifying the spatial pattern of the initial errors that can cause a significant SPB
- Exploring the physical mechanisms of the SPB from the perspective of error growth

Correspondence to:

W. Duan,
duanws@lasg.iap.ac.cn

Citation:

Liu, D., Duan, W., Feng, R., & Tang, Y. (2018). Summer predictability barrier of Indian Ocean dipole events and corresponding error growth dynamics. *Journal of Geophysical Research: Oceans*, 123. <https://doi.org/10.1029/2017JC013739>

Received 28 DEC 2017

Accepted 20 APR 2018

Accepted article online 30 APR 2018

Summer Predictability Barrier of Indian Ocean Dipole Events and Corresponding Error Growth Dynamics

Da Liu^{1,2}, Wansuo Duan^{1,2} , Rong Feng¹, and Youmin Tang³ 

¹State Key Laboratory of Numerical Modeling for Atmospheric Sciences and Geophysical Fluid Dynamics, Institute of Atmospheric Physics, Chinese Academy of Sciences, Beijing, China, ²College of Earth and Planetary Sciences, University of Chinese Academy of Sciences, Beijing, China, ³Environmental Science and Engineering, University of Northern British Columbia, Prince George, Canada

Abstract The effects of sea temperature errors in both tropical Pacific and Indian oceans on the predictability of positive Indian Ocean dipole (IOD) events are explored by using the GFDL CM2p1 coupled model. The results show that the positive IOD events tend to occur with a “winter predictability barrier” (WPB) and a “summer predictability barrier” (SPB). More is known about the WPB, while less is known about the SPB. This study focuses on the SPB. The results demonstrate that two types of initial errors are more likely to cause a significant SPB. One type is of large and negative sea surface temperature anomalies (SSTAs) in the central-eastern Pacific and a dipole mode-structured subsurface sea temperature that has negative anomalies in the upper layers of the eastern equatorial Pacific and positive anomalies in the lower layers of the western equatorial Pacific; the other type shows a pattern almost opposite of the former type. By tracking evolutions of both types of initial errors, it is found that their Pacific Ocean (PO) component-induced northwesterly wind in the east pole of IOD is significantly suppressed by the summer strongest climatological southeasterly and positive IOD-induced southeasterly wind there, finally causing the considerable suppression of the loss of latent heat flux in the east pole and then favors the fastest growth of a positive SST error in this region during summer. Then a significant SPB for the IOD occurs.

1. Introduction

The Indian Ocean dipole (IOD) is one of the dominant modes in the tropical Indian Ocean (IO) at the interannual time scale (Saji et al., 1999; Saji & Yamagata, 2003a; Webster et al., 1999). The IOD presents positive and negative phases. The positive IOD (pIOD) is featured with positive sea surface temperature anomalies (SSTAs) in the western IO (WIO) and negative SSTAs in the southeast IO (SEIO), while the negative IOD (nIOD) shows an almost opposite pattern (Murtugudde et al., 2000; Saji et al., 1999). The dipole mode index (DMI), which is defined by the difference in SSTAs between the WIO and the SEIO, is usually used to measure the intensity of IOD events (Saji et al., 1999). If the DMI exceeds 0.5 standard deviations for three consecutive months, an IOD event occurs (Song et al., 2007). IOD events usually grow in boreal summer, then peak in fall and collapse rapidly in winter (Saji et al., 1999; Saji & Yamagata, 2003a; Webster et al., 1999). Such development of SSTAs would cause precipitation anomalies in east Africa, Indonesia, and Australia (Ashok et al., 2001; Birkett et al., 1999; Clark et al., 2003). The IOD also affects temperature and rainfall in Europe, Asia, and South America through planetary waves (Annamalai & Murtugudde, 2004; Ansell et al., 2000; Black et al., 2003; Saji & Yamagata, 2003b). Since the IOD has a significant influence on global weather and climate, it is very important to predict IOD events successfully.

The IO and the Pacific Ocean (PO) play dominant roles in the tropical oceans. In addition, the IOD and the El Niño Southern Oscillation (ENSO) are the most significant interannual variability occurred in the IO and PO, respectively (Bjerknes, 1969; Philander, 1983, 1990; Saji et al., 1999; Webster et al., 1999). Stuecker et al. (2017) found that only a small fraction (approximately 32%) of IOD events occur independently of ENSO events (also see Loschnigg et al., 2003; Saji et al., 1999), which suggests that the IOD is closely related to ENSO. Previous studies indicated that ENSO could affect the IOD through the Walker circulation, South Asian monsoon, and convection over the maritime continent (Li et al., 2003), among which, the effect of the Walker circulation was particularly emphasized (Alexander et al., 2002; Chen, 2011; Wang & Wang, 2014; Zhang et al., 2015). During El Niño, the Walker circulation is weakened, with anomalous divergence

occurring over the Indo-Pacific region, and surface easterly anomalies near Sumatra enhance oceanic upwelling, which favors the occurrence of the IOD (Yu & Lau, 2005; Zhang et al., 2015). Thus, ENSO is one of the external drivers that could induce the occurrence of IOD events (Li et al., 2003).

From the perspective of predictions and predictability, Ding and Li (2012) showed that El Niño-induced atmospheric circulation changes cause the sign of SSTAs in the WIO (and in the SEIO) to be reversed during spring (and winter), which makes the corresponding autocorrelation of the SSTAs drop quickly during this season and indicates the occurrence of the spring (winter) persistence barrier of SSTAs in the WIO (and the SEIO) (also see Luo et al., 2007; Wajsowicz, 2005, 2007). The persistence barrier also exists in IOD events. Nevertheless, Feng et al. (2014b) found that the autocorrelation of the IOD-related DMI declines rapidly in winter only and indicated that only the winter persistence barrier exists in IOD events. The persistence barriers may limit the prediction skill of IOD events, which may lead to the occurrence of the predictability barrier. By calculating anomaly correlation coefficients between the observations and predictions, Luo et al. (2007) demonstrated that the anomaly correlation coefficients decrease rapidly during winter and the IOD occurs with a winter predictability barrier (WPB) phenomenon. From the perspective of error growth, Feng and Duan (2014) found that prediction errors (or root-mean-square errors, RMSE) for IOD events, whenever the predictions start, tend to have significant growth during the boreal winter season and induce the WPB phenomenon for IOD predictions. That is, IOD prediction skills measured by either the anomaly correlation coefficient or the RMSE decline rapidly in winter and occur the WPB phenomenon. The WPB could be essential for IOD predictions.

With the Geophysical Fluid Dynamics Laboratory (GFDL) CM2p1 coupled model, Feng and Duan (2014) and Feng et al. (2014a) studied the effect of IO initial errors on the WPB for IOD predictions. They demonstrated that vertical temperature advection associated with IOD events, along with latent heat flux and shortwave radiation, favor the season-dependent evolution of error growth for IOD events. The WPB did not exist in every IOD prediction; therefore, Feng and Duan (2014) showed that, apart from climatological conditions, the spatial patterns of initial errors also play a key role in the occurrence of the WPB. Feng and Duan (2014) found that the WPB for IOD events is closely related to particular spatial patterns of initial sea temperature errors in the Indian Ocean. In particular, they showed that an IO initial sea surface temperature error with a dipole pattern is more likely to cause a significant WPB. However, when the present study analyzes the effect of the tropical PO and IO sea temperature errors on IOD predictions, it concludes that IOD predictions encounter summer predictability barrier (SPB) as well as the prementioned WPB (see section 3). For the SPB, we naturally question the source of the prediction errors associated with the SPB for IOD events, and whether there are initial errors with a particular pattern that are more likely to cause the SPB. We also question the physical mechanism that causes the SPB.

To address these questions, we conduct perfect model predictability experiments, where the prediction errors are only caused by initial errors. The remainder of this paper is organized as follows: the model and related experimental strategy are described in section 2. In section 3, the predictability barriers of IOD events are revealed, and the initial errors that most likely induce a significant SPB are identified. The mechanisms responsible for the SPB of the IOD are discussed in section 4. Finally, a summary and discussion are presented in section 5.

2. Model and Experimental Strategy

The model used in the present study is the GFDL CM2p1 coupled model. The simulations of the IO climatology and IOD generated by this model have been evaluated against the Simple Ocean Data Assimilation data set (SODA 2.2.4, reanalysis data; Carton & Giese, 2008). The GFDL CM2p1 coupled model is found to present good simulation to the IO climatology (including sea temperature and wind components) and the essential features of IOD events. Especially, Feng et al. (2014b) compared 14 models in the Coupled Model Intercomparison Project phase 5 (CMIP5) and found that the GFDL CM2p1 coupled model is one of the models of the highest simulation skill. Because the comparison between the GFDL CM2p1 coupled model output and the SODA data was also made in Feng et al. (2014b), the figures are omitted here and the details can be seen in Feng et al. (2014b). From these comparisons, it is clear that the GFDL CM2p1 coupled model can be a platform for studying the IOD and its related predictability. The GFDL CM2p1 coupled model is a fully coupled model with ocean, atmosphere, land, and sea ice components. The ocean component of the

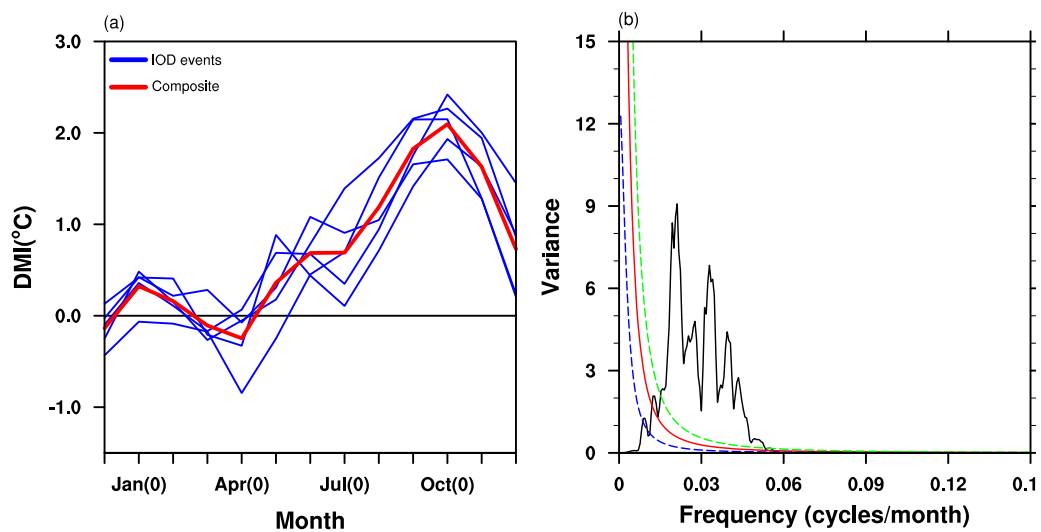


Figure 1. (a) Time-dependent DMI for the five IOD events in the GFDL CM2p1 coupled model. The five blue curves represent the five IOD events, and the red curve represents the composite of the five IOD events. (b) The power spectrum analysis of DMI in the GFDL CM2p1 coupled model. The calculations are for the last 150 years of the 200 year control simulation in the model. The frequency of the largest variances is about 0.025, which corresponds to a period of 4 years. The red solid line represents the Markov "Red Noise" spectrum, the blue and green dash lines are the lower and higher confidence bound for Markov with the given 95% confidence degree.

GFDL CM2p1 coupled model is the Modular Ocean Model version 4 (MOM4p1), which is a numerical representation of the ocean's hydrostatic primitive equations. The resolution of the MOM4p1 is $1^\circ \times 1^\circ$ in most regions, and the meridional resolution is reduced to $1/3^\circ$ near the equator. There are 50 vertical levels, with a 10 m resolution in the upper 225 m. The atmospheric component is the GFDL atmosphere model (AM2p12b). Its horizontal resolution is 2° latitude by 2.5° longitude with 24 vertical levels. The MOM4p1 and AM2p12b are coupled with the Land Dynamics model version 2.1 (LM2.1; Milly & Shmakin, 2002) and the GFDL Sea Ice Simulator (SIS; Delworth et al., 2006) through the GFDL's Flexible Modeling System (FMS, <http://www.gfdl.noaa.gov/fms>); each component exchanges fluxes every 2 h. More details can be found in Delworth et al. (2006) and Griffies (2009).

To study the effects of initial errors on IOD prediction uncertainties, we conducted perfect model predictability experiments within the frame of the GFDL CM2p1 coupled model. That is, the model is assumed to be perfect, and the prediction errors of IOD events are only caused by initial errors. In these perfect model predictability experiments, the GFDL CM2p1 coupled model is run for 200 years and forced by values for land cover, aerosols, tracer gases, and insolation in 1990. After a 50 year spin-up period, the last 150 years are analyzed. The climatological annual cycle is calculated for the whole period of the 150 year control run, and the anomalies are obtained by subtracting the climatological annual cycle from the monthly data generated by the model, consequently presenting pIOD and nIOD events. The pIOD events are usually stronger than the nIOD events, and their influences on weather and climate anomalies are, therefore, much more serious. Furthermore, under global warming scenarios, the frequency of the occurrence of the pIOD has been found to be increasing obviously (Ashok et al., 2001, 2003; Black et al., 2003; Cai et al., 2009; Guan & Yamagata, 2003; Hong et al., 2008). Therefore, in the present study, we mainly focus on the predictability of pIOD events.

Figure 1a shows the DMI of five typical pIOD events chosen from the 150 year integrations as the "true state." It is shown that the sign of the DMI is reversed from negative to positive in late winter or early spring, then the DMI increases in summer, peaks in September or October, and declines rapidly in the following months. In addition, by observing the power spectral of the time series of the 150 year DMI, the dominant period of IOD events in the GFDL CM2p1 is found to be about 4 years (see Figure 1b). All of these results are consistent with the observations (Mu & Li, 2002; Saji & Yamagata, 2003a), and the GFDL CM2p1 is acceptable for investigating IOD predictability.

The initial errors are superimposed on the initial sea temperature for the five "true state" IOD events. The initial errors are generated by taking the differences between the sea temperature of the "true state" at the

start month and that in each month in the 4 years preceding the start month. For each event, we attained 48 initial errors for one start month. Since the dominant period of the IOD is approximately 4 years in the GFDL CM2p1 coupled model, the patterns of sea temperature anomalies within 4 years may be responsible for much ergodic initial errors. Due to these initial errors, for each IOD event we make 18 month predictions, with the start month being April (−1) and July (−1), and 12 month predictions, with the start month being October (−1) and January (0) ("0" denotes the IOD year when the IOD attains peak, and "−1" represents the year preceding the IOD year). In total, there are 960 predictions for the five IOD events, with 240 predictions for each start month. In these prediction experiments, the initial errors of the sea temperature cover the region (15°N–15°S, 50°E–85°W) from the surface to a 225 m depth and simultaneously consider the tropical Indian and Pacific oceans, which encourages us to study the effects of uncertainties occurring in sea temperatures, both in the tropical Pacific and Indian oceans, on the predictability of IOD events.

To study the evolution of the initial error, the prediction error is defined as the absolute value of the difference between the predicted DMI and the DMI of "true state" IOD events. Specifically, it can be expressed as follows in equation (1):

$$\text{DMI}'(t) = |\text{DMI}^P(t) - \text{DMI}^I(t)|, \quad (1)$$

where the $\text{DMI}^P(t)$ and $\text{DMI}^I(t)$ are the predicted DMI and the true DMI, respectively, at lead time t , and $\text{DMI}'(t)$ is the prediction error caused by the initial errors. Then, the growth tendency κ of the prediction errors at each month can be calculated by using $\kappa = \frac{\partial \text{DMI}'(t)}{\partial t}$. As an approximation, the monthly growth tendency of the prediction errors can be written as follows in equation (2):

$$\kappa(t) = \text{DMI}'(t+1) - \text{DMI}'(t), \quad (2)$$

where the time t is the initial time for a month, and $t + 1$ denotes the final time of the month. A positive (negative) value of κ indicates an increase (decrease) in the prediction errors, and the larger the absolute value of κ , the faster the increase (decrease) in errors. Therefore, the growth tendency κ can indicate the change in prediction skill for 1 month. By taking the sum of 3 monthly growth tendencies in one season, the total growth tendency of the prediction errors during the season can certainly be described, which then measures the seasonal growth rate of the prediction errors and indicates the change of prediction skill during the season. If the sum of monthly growth tendency κ during a season is positive (negative), the prediction errors increase (decrease), and the prediction skill decreases (increases) in this season; the larger the absolute value of the sum, the faster the decrease (increase) in the prediction skill.

3. The Summer Predictability Barrier (SPB) of IOD Events and Two Types of SPB-Related Initial Errors

We divide the calendar year into four seasons, starting with January to March (JFM), followed by April to June (AMJ), July to September (JAS), and October to December (OND), and investigate the season-dependent evolution of prediction errors for IOD events. According to the experimental strategy, we take the predetermined initial errors and superimpose them onto the initial states for the chosen five IOD events (see section 2), then integrate the model for 18 months from the start months (i.e., April (−1) and July (−1)) and 12 months from the start months (i.e., October (−1) and January (0)) to obtain predictions for the IOD events. Therefore, the prediction errors can be derived by taking the difference between the "true state" IOD events and their predictions. Figure 2 shows the ensemble mean of the seasonal growth rates of prediction errors for 240 predictions starting from the start months of April (−1), July (−1), October (−1), and January (0) (see section 2). It is shown that the IOD predictions, except for those starting in October (−1), tend to have considerable growth in both JFM and JAS seasons, which indicates that prediction skills often significantly decrease during winter and summer. In the introduction, the winter predictability barrier (WPB) for the IOD events is referred to as the fast growth of prediction errors in winter. Similarly, for the significant growth of prediction errors for IOD events during summer, we can think that the IOD predictions encounter the summer predictability barrier (SPB). Therefore, the results shown in Figure 2 indicate the occurrence of the WPB and SPB for IOD events.

The WPB for IOD predictions was reported by previous studies (Feng & Duan, 2014; Feng et al., 2014a; Luo et al., 2007). Feng et al. (2014a) showed that the seasonality of vertical temperature advection, latent heat

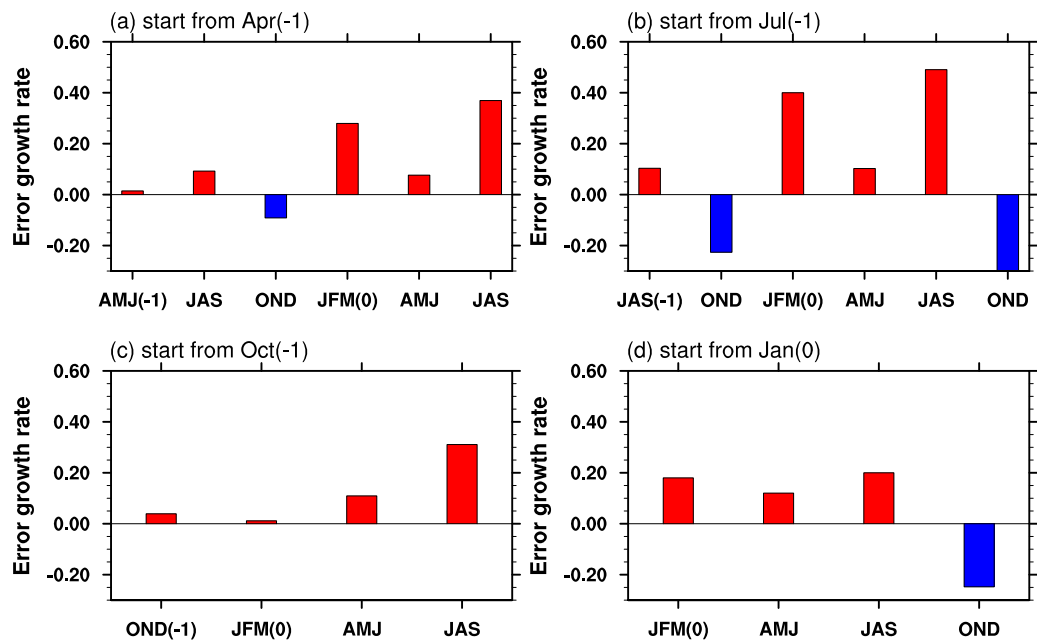


Figure 2. Histograms of seasonal growth rate κ for prediction errors for IOD events, which are calculated by taking the ensemble mean of seasonal growth rates κ of the 240 predictions for each start month for the five IOD events. The predictions include four start months: (a) April (-1), (b) July (-1), (c) October (-1), and (d) January (0).

flux, and shortwave radiation favor the season-dependent evolution of prediction errors for IOD events. Feng and Duan (2014) also demonstrated that initial sea temperature errors of a dipole mode occurring in the IO are favorable for the occurrence of the WPB; particularly, they illustrated that IO subsurface sea temperature errors make a larger contribution to prediction errors for IOD events. However, for the SPB of IOD events, little is known about it, despite Luo et al. (2007) also acknowledged the existence of the SPB in IOD predictions.

In this study, we focus on the SPB and its physical mechanisms. For this, we choose the IOD predictions that occur with a significant SPB. The significant SPB here is referred to the phenomenon that a prominent error growth occurs during summer when the prediction is made before the summer. To specify the “prominent,” we take the differences between the largest error growth rate and the second largest one for the IOD predictions with a SPB as a group of samples. Then we particularly select the predictions with the differences being more than 1.5 standard deviations of the samples. Upon this request, we identify 294 IOD predictions from the 960 predictions for the five IOD events. These 294 predictions occur with a significant SPB and include 81 predictions for the starting month of April (-1), 114 for the starting month of July (-1), 61 for the starting month of October (-1), and 38 for the starting month of January (0). For these predictions, prediction errors are only caused by initial sea temperature errors occurring in the IO and PO because the model is assumed to be perfect (see section 2). For convenience, we call the initial errors of the above 294 predictions as SPB-related initial errors. Obviously, the SPB-related initial errors refer to as the ones that are superimposed on the month when the predictions start and whose evolutions exhibit prominent growth during summer and present a significant SPB phenomenon. For these 294 SPB-related initial errors, we remove their related IO and PO components, superimpose them on “true state” IOD events, conduct predictability experiments, then finally compare the contribution of IO and PO components of the SPB-related initial errors to the SPB. Figure 3 shows the ensemble mean for the growth tendencies of prediction errors caused by the IO and PO components of the SPB-related initial errors for five IOD events, correspondingly. The results show that whenever predictions start, the prediction errors caused by the PO component of the SPB-related initial errors always have the largest growth tendencies in JAS, while those caused by the IO component exhibit the largest growth tendencies in JFM. That is, the IO component of the SPB-related initial errors tends to cause a WPB, while the PO component is inclined to yield an SPB. Feng and Duan (2014) and Feng et al. (2014a) only emphasized initial sea temperature errors occurring in the IO and

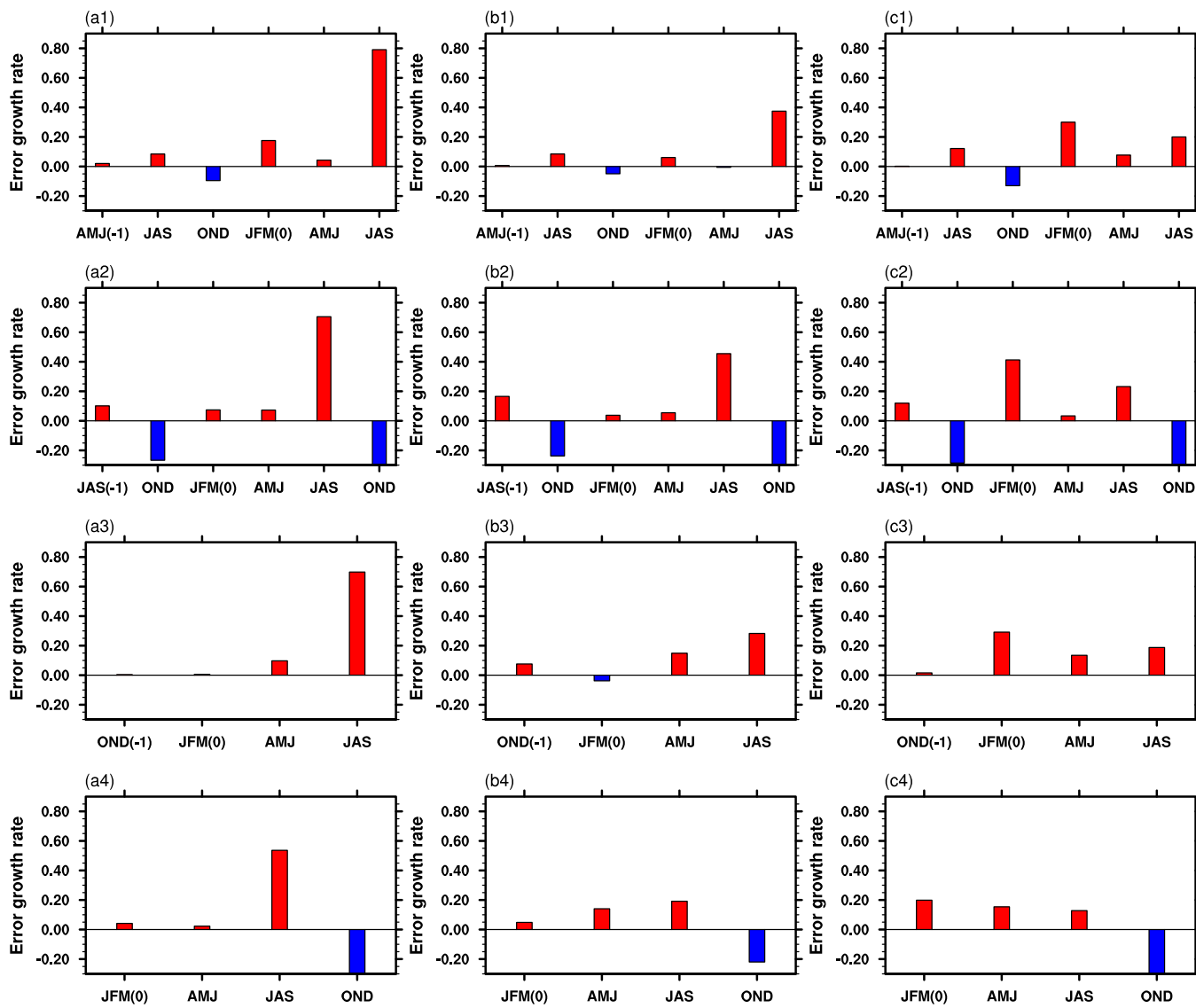


Figure 3. Histograms of the seasonal growth rate κ for (a) SPB-related initial errors and the corresponding (b) PO and (c) IO components. They are calculated by taking the ensemble mean of κ for the SPB-related initial errors for (1) 81 predictions with the start month of April (-1), (2) 114 predictions with the start month of July (-1), (3) 61 predictions with the start month of October (-1) and (4) 38 predictions with the start month of January (0).

demonstrated that they cause a significant WPB for IOD events. Obviously, the results derived by the IO component of the SPB-related initial errors in this study support the conclusion obtained by Feng and Duan (2014) and Feng et al. (2014a). Additionally, this study further illustrates the SPB for IOD predictions and identifies the main error source of the SPB. The initial sea temperature errors occurring in the PO contribute to the SPB for IOD events. That is, the prediction errors associated with the SPB mainly come from the PO, and the prediction errors related to the WPB come from the IO. As mentioned in the introduction, Feng and Duan (2014) and Feng et al. (2014a) explained that the physical mechanisms of the WPB and identified initial IO sea temperature errors are much more likely to cause a significant WPB. Now, we focus on the SPB and explore the features of the SPB-related initial errors that occur in both the IO and PO, despite their PO component, which contributes more to the SPB.

For the above 294 SPB-related initial errors, we performed a combined empirical orthogonal function (CEO) analysis to their sea temperature component with an array of (latitude, longitude, level, 294), where the latitude is from 15°S to 15°N , the longitude is from 50°E to 85°W covering both PO and IO, and the level is from sea surface to a depth of 225 m. To explore the principal characteristics of the initial errors that

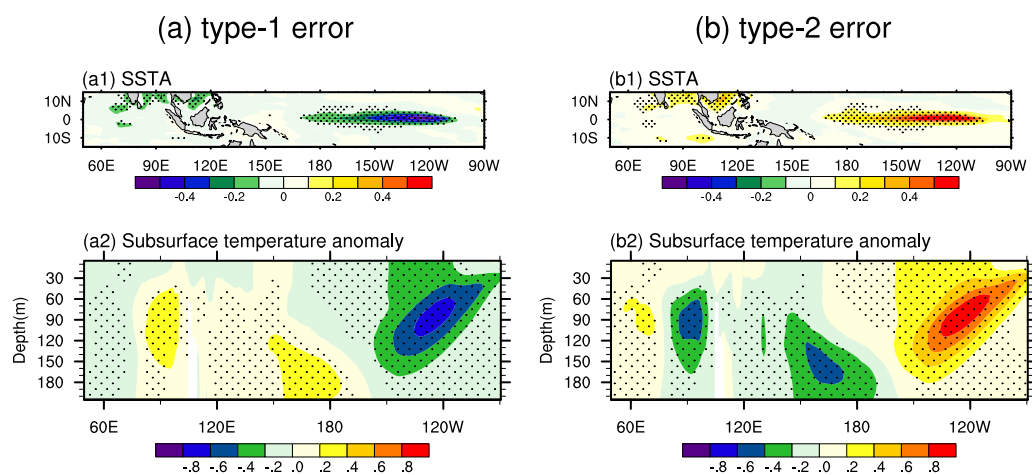


Figure 4. Composites for (a) type-1 initial errors and (b) type-2 initial errors that cause a significant SPB for IOD predictions. The top plot shows the SSTA component, and the bottom plot shows the equatorial subsurface temperature anomaly (units: $^{\circ}\text{C}$, averaged over the region 5°S – 5°N). Dotted areas indicate that the composites for SSTA and subsurface temperature anomaly errors exceed the 99% significance level with a *t* test.

cause a significant SPB, we cared about the dominant mode of the 294 SPB-related initial errors. Correspondingly, we extracted the dominant CEOF1 mode that explains 29.7% of the total variance and the related principle component (PC1). The PC1 presented a series of 294 points (corresponding to 294 SPB-related initial errors) with positive and negative values and indicated that the dominant mode of SPB-related initial sea temperature errors exhibited either a CEOF1 pattern or the opposite pattern. To classify the original SPB-related initial errors, we went back to the original 294 SPB-related initial errors and, according to the positive and negative values of PC1, divided them into two groups, with 159 errors in the first group that corresponded to the positive PC1, and the remaining 135 in the second group corresponded to the negative PC1. We took respectively the composite of these two groups of initial errors and obtained two types of initial error patterns for SSTAs and subsurface temperature anomalies around the equator (Figure 4). The largest values for both types of initial errors were located in the PO, which illustrated that the prediction errors associated with the SPB were closely related to initial errors in the PO. Specifically, the first type was featured with large negative SSTAs in the central-east tropical PO, a dipole mode with negative anomalies in the upper layers of the eastern equatorial Pacific and positive anomalies in the lower layers of the western equatorial Pacific (Figure 4a; hereafter known as type-1 initial errors). The second type showed almost the opposite pattern of the type-1 initial errors and is referred to as type-2 initial errors (Figure 4b). For a given start month, the IOD predictions with a SPB are possible to have not only type-1 but also type-2 errors (see Table 1). Furthermore, they, whichever start month the IOD predictions were initialized at, finally induced negative prediction errors of the DMI index of IOD in summer, with positive SST errors occurring in the east pole (10°S – 0° , 90°E – 110°E) of the IOD and negative SST errors occurring in the west pole (10°S – 10°N , 50°E – 70°E) of the IOD (see Figures 5 and 6; an example of the start month October (–1)). Such prediction errors mean that the true state pIOD events were weakened or even turned into negative IOD events for predictions with the effect of the type-1 and type-2 initial errors. The differences between the evolutions of two types of initial errors existed mainly in the PO, especially before summer. The type-1 errors showed negative SST errors in the PO and, whichever start month they were initialized at, finally evolved into a La Niña-like mode there. Obviously, this process presented a positive feedback from initially negative SST errors to finally negative SST prediction errors in the PO in summer.

The type-2 errors exhibited positive SST errors in the PO but they also evolved into a La Niña-like mode in the PO in summer. They certainly underwent a negative feedback from initially positive SST error to eventually negative SST prediction errors in the PO in summer. These differences between the type-1 and type-2 errors mainly occurred during the initial period of their evolutions in the PO and the corresponding errors were of relatively small amplitude. This may cause

Table 1
Number of Type-1 and Type-2 Errors Occurring at Each Start Month

Type	Apr (–1)	Jul (–1)	Oct (–1)	Jan (0)
Type-1	44	62	33	20
Type-2	37	52	28	18

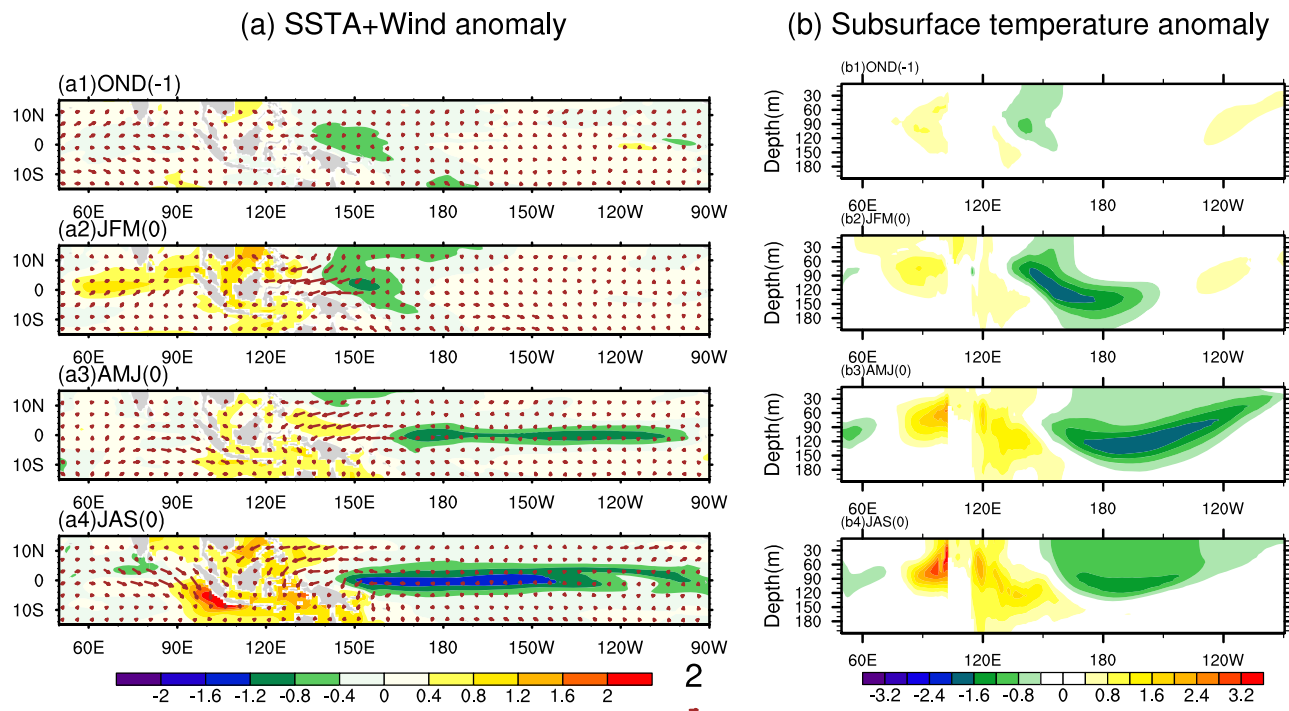


Figure 5. (a) Composites of seasonal mean of tropical SSTAs (units: °C) and surface wind anomaly (units: m/s) for prediction errors caused by the type-1 initial errors for the five IOD events. (b) As in Figure 5a, but for the equatorial subsurface temperature anomaly (units: °C; averaged over 5°S by 5°N). This figure, as an example, shows the prediction errors for the predictions with start month October (−1).

that the PO component of the evolutions of type-1 and type-2 errors had a small effect on the IO component during the initial period, which then makes the IO component possessed quite similar evolution for type-1 and type-2 errors.

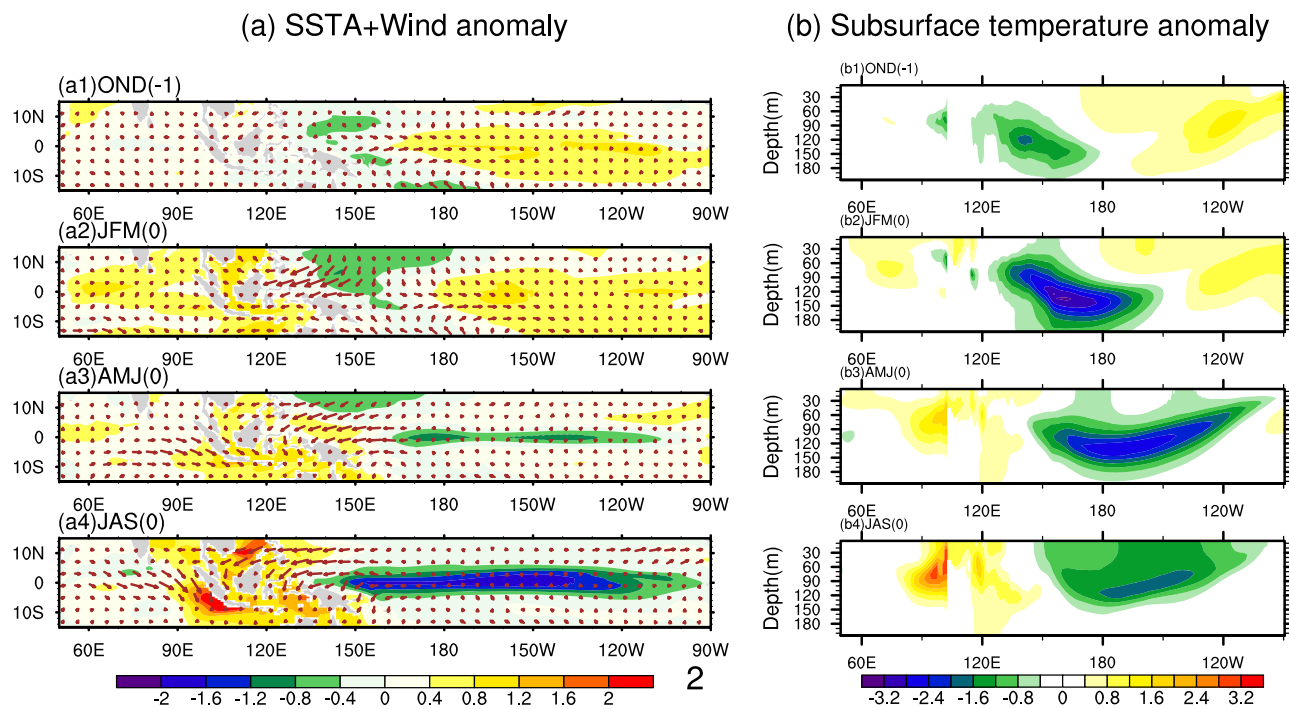


Figure 6. As in Figure 5, but for the type-2 initial errors.

4. Dynamic Mechanisms of the Error Growth Related to the SPB for IOD Events

In this section, we explore the dynamic mechanisms responsible for the SPB by studying the sea temperature tendency equation associated with SPB-related initial errors. The sea temperature tendency equation is as follows:

$$\frac{\partial T}{\partial t} = -u \frac{\partial T}{\partial x} - v \frac{\partial T}{\partial y} - w \frac{\partial T}{\partial z} + \frac{1}{\rho C_p} \frac{\partial Q}{\partial z} + \kappa \nabla^2 T, \quad (3)$$

where T is the sea temperature; u , v , and w are the zonal, meridional, and vertical current velocities, respectively; ρ is the sea water density, which is set to 1,038 kg/m³; C_p is the specific heat of sea water, which has a value of 4,000 J/(kg°C); and κ is the mixing coefficient. We rewrite the state variables in this equation into two terms with the form $X = \bar{X} + X^*$, where \bar{X} represents the climatological mean of X , and X^* signifies the anomaly superimposed on \bar{X} (i.e., the SST anomaly of the reference state IOD event). Then, equation (3) can be formulated, as shown in equation (5). If we further consider equation (3) as the forecast model with prediction errors, then equation (3) can be rewritten as shown in the equation (4) by $X = \bar{X} + X^* + X'$, where X' denotes the errors of the state variable X . Subtracting equation (5) from equation (4) gives equation (6), which describes the tendency of the evolution of prediction errors caused by initial errors. The terms A and B in equation (6) describe the effects of the climatological mean and the reference state IOD event, respectively, on prediction errors of sea temperature; \bar{u} , \bar{v} , and \bar{w} represent the climatological mean of the zonal, meridional and vertical current velocities, respectively, and u^* , v^* , and w^* represent the anomalous current velocities of the IOD events, respectively. The term C is formulated by the errors themselves and depicts the effect of perturbed temperature advection on sea temperature prediction errors; u' , v' , and w' represent the errors of the anomalous current velocities for IOD events. The term Q is also related to the errors themselves, but it describes the combined effect of the errors for shortwave radiation, longwave radiation, sensible heat flux, and latent heat flux on the prediction errors of sea temperature. The term R is the residual term that includes mixing terms and truncation errors.

$$\begin{aligned} \frac{\partial(\bar{T} + T^* + T')}{\partial t} = & -(\bar{u} + u^* + u') \frac{\partial(\bar{T} + T^* + T')}{\partial x} - (\bar{v} + v^* + v') \frac{\partial(\bar{T} + T^* + T')}{\partial y} \\ & - (\bar{w} + w^* + w') \frac{\partial(\bar{T} + T^* + T')}{\partial z} + \frac{1}{\rho C_p} \frac{\partial(\bar{Q} + Q^* + Q')}{\partial z} \\ & + \kappa \nabla^2(\bar{T} + T^* + T') \end{aligned} \quad (4)$$

$$\begin{aligned} \frac{\partial(\bar{T} + T^*)}{\partial t} = & -(\bar{u} + u^*) \frac{\partial(\bar{T} + T^*)}{\partial x} - (\bar{v} + v^*) \frac{\partial(\bar{T} + T^*)}{\partial y} - (\bar{w} + w^*) \frac{\partial(\bar{T} + T^*)}{\partial z} \\ & + \frac{1}{\rho C_p} \frac{\partial(\bar{Q} + Q^*)}{\partial z} + \kappa \nabla^2(\bar{T} + T^*) \end{aligned} \quad (5)$$

$$\frac{\partial T'}{\partial t} = A + B + C + Q + R \quad (6)$$

where

$$A = -\bar{u} \frac{\partial T'}{\partial x} - \bar{v} \frac{\partial T'}{\partial y} - \bar{w} \frac{\partial T'}{\partial z} - u' \frac{\partial \bar{T}}{\partial x} - v' \frac{\partial \bar{T}}{\partial y} - w' \frac{\partial \bar{T}}{\partial z},$$

$$B = -u^* \frac{\partial T'}{\partial x} - v^* \frac{\partial T'}{\partial y} - w^* \frac{\partial T'}{\partial z} - u' \frac{\partial T^*}{\partial x} - v' \frac{\partial T^*}{\partial y} - w' \frac{\partial T^*}{\partial z},$$

$$C = -u' \frac{\partial T'}{\partial x} - v' \frac{\partial T'}{\partial y} - w' \frac{\partial T'}{\partial z},$$

$$Q = \frac{1}{\rho C_p} \frac{\partial Q'}{\partial z}.$$

As mentioned in the last section, the type-1 and type-2 initial errors for pIOD events tend to cause positive SST errors occurring in the east pole of the IOD but negative SST errors occurring in the west pole of the

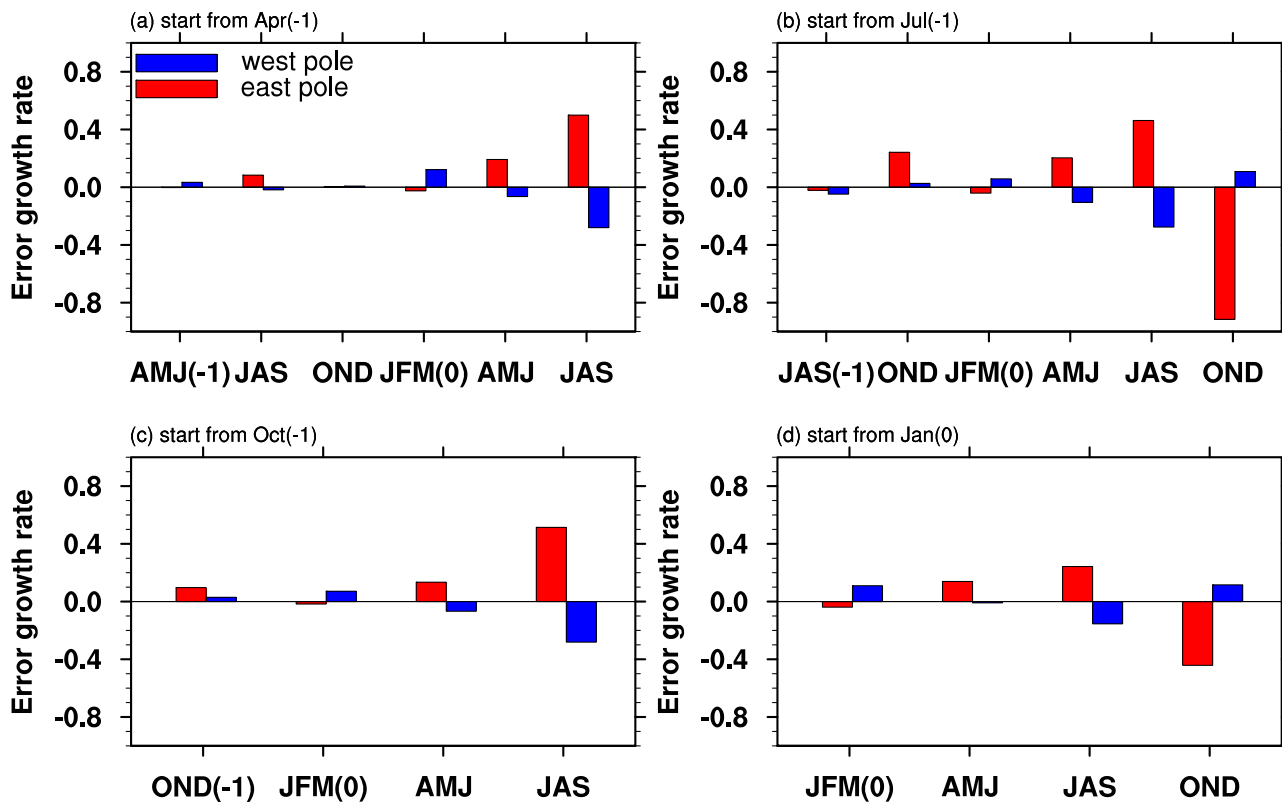


Figure 7. Histograms of the growth rate for the east pole and west pole SST component of the IOD prediction error caused by SPB-related initial errors, with the start month for prediction being (a) April (−1), (b) July (−1), (c) October (−1), and (d) January (0).

IOD, which presents a nIOD-like evolutionary behavior (see Figures 5 and 6). We investigate the seasonal growth rate of the prediction errors of SSTs in the east and west poles and find that the former presents a significant season-dependent evolution, with the fastest error growth rate in summer (Figure 7). Although the latter also exhibits a season-dependent evolution, its error growth rate during summer is negative, which indicates that the prediction errors tend to decrease in summer. However, considering that the IOD prediction errors measured by the DMI have a significant SPB, we think that the summer negative growth rate of prediction errors of the SSTs in the west pole further emphasizes the dominant role of the seasonality of the prediction errors of SSTs in the east pole in the SPB for the IOD. Therefore, to identify which mechanisms are mainly responsible for the occurrence of the SPB, we focus on the season-dependent evolutionary dynamics of the SST errors in the east pole of the IOD. It is clear from the equation (6) that the terms with positive values favor the growth of positive SST errors in the east pole, and those with negative values suppress the growth of positive SST errors. In fact, we find that the terms $-\bar{u} \frac{\partial T'}{\partial x}$, $-u^* \frac{\partial T'}{\partial x}$, and $-v \frac{\partial T'}{\partial y}$ and latent heat flux error ($\frac{-1}{\rho C_p} \frac{\partial Q'}{\partial z}$) present positive values in summer. Specifically, we find that values for the $-u^* \frac{\partial T'}{\partial x}$ term and the latent heat flux errors are much larger than the other two terms in summer, which are, therefore, much more favorable for the growth of positive SST errors in the east pole in summer than in other seasons (Figure 8). However, in terms of seasonality, latent heat flux errors present obvious seasonality and show to be positive and large in summer but small or negative in other seasons, while the term $-u^* \frac{\partial T'}{\partial x}$ is positive and large not only in summer, but also in subsequent seasons (see Figures 8b and 8d). Obviously, the large and positive latent heat flux during summer especially enhances the growth of positive SST errors in the east pole of the IOD and tends to induce a significant SPB for IOD. Therefore, it is questioned why the latent heat flux associated with the prediction errors of SSTs in the east pole of the IOD is large and positive during summer.

We still took the predictions with start month October (−1) as example to explain the above question. For other predictions with start months being April (−1), July (−1), and January (0), we can adopt similar thinking to address the above question. In fact, latent heat flux errors essentially come from type-1 and type-2

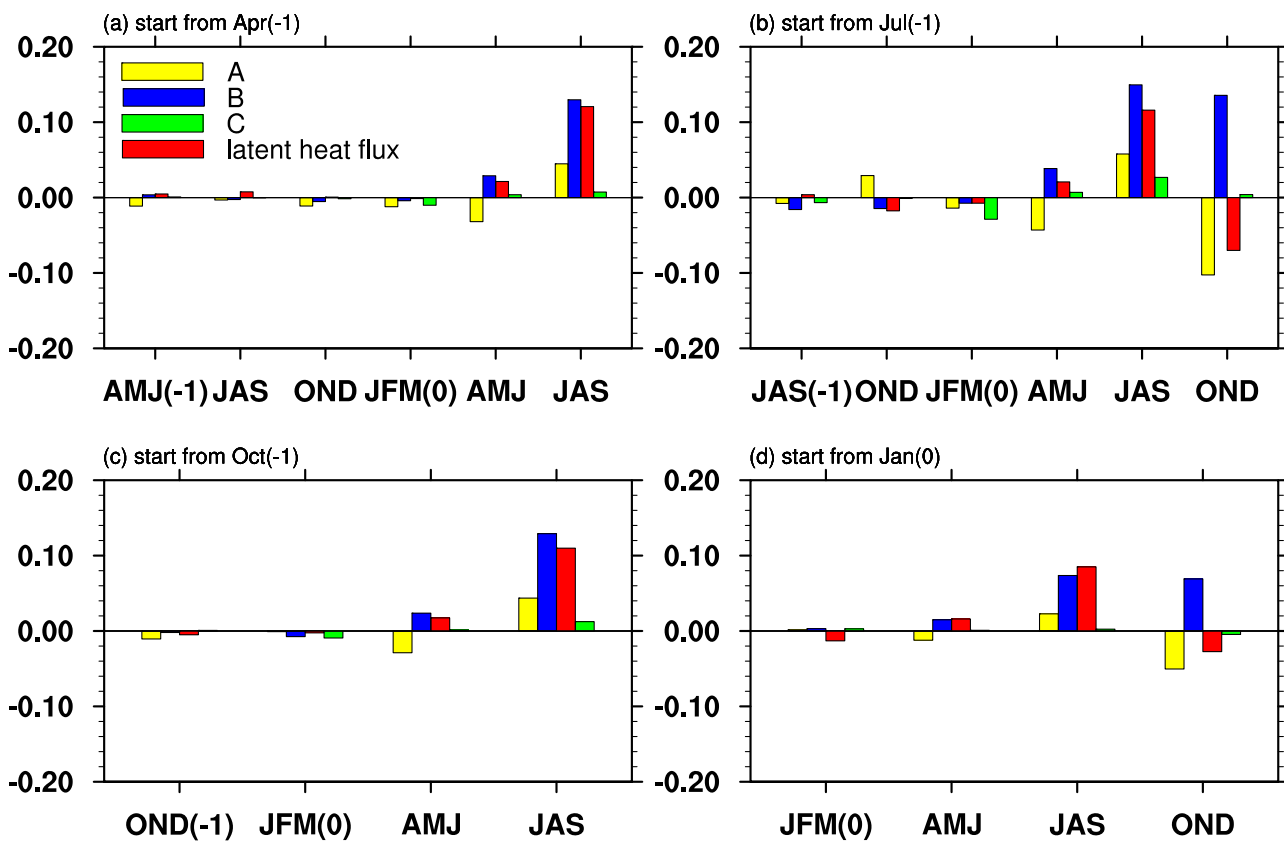


Figure 8. Seasonal mean of the terms $-\bar{u} \frac{\partial T'}{\partial x}$ (denoted by A), $-u^* \frac{\partial T'}{\partial x}$ (denoted by B), $-\bar{v} \frac{\partial T'}{\partial y}$ (denoted by C) and latent heat flux ($\frac{1}{\rho C_p} \frac{\partial Q_L}{\partial z}$) in equation (6), where the start months are (a) April (-1), (b) July (-1), (c) October (-1), and (d) January (0). Particularly, the positive values of latent heat flux term indicate the suppression of the loss of the latent heat flux and the negative values mean the enhancement of the loss of the latent heat flux.

initial sea temperature errors. From Figures 5 and 6, it is shown that the evolutions of two types of initial errors are different during the initial period, but eventually both of them exhibit a La Niña-like mode in the PO and nIOD-like mode in the IO in summer. That is to say, both type-1 and type-2 errors finally cause negative SST errors in the PO and positive SST errors in the eastern IO in summer despite they undergoes somewhat different behaviors in other seasons. The negative errors in the PO induce anomalous easterlies occurring in the PO; simultaneously, due to the existence of the double-cell Walker circulation over the Indo-Pacific oceans and its gear effect (Chen, 2011; Wu & Meng, 1998), an anomalous westerly occurs in the IO; more particularly, an anomalous northwesterly wind occurs in the east pole of the IOD at 1 year lead time. It is known that wind speed $|v_a|$ is positively correlated with latent heat flux, $Q_L = \rho_a L_E C_E |v_a| (q_a - q_s(T_s))$ (Cayan, 1992). That is, the wind can determine the loss or absorption of latent heat flux. In fact, the climatological mean state tends to present the westerly component in the east IO during winter (i.e., the JFM season in the present study) and autumn (i.e., the OND season), and the southeasterly during spring (i.e., the AMJ season) and summer (i.e., the JAS season), with that in summer being much stronger (see Figures 9 and 10). For type-1 errors, their northwesterly wind anomalies in the east IO are suppressed by much stronger climatological southeasterly during summer, which decreases the loss of latent heat flux and finally causes latent heat flux in the equation (6) to be positive (see Figure 11) and enhance the growth of the positive SST errors in the east IO. However, during other seasons, the climatological mean exhibits winds different from those in summer, which has different effects on latent heat flux. Specifically, during spring, the climatological mean also presents southeasterly in the east IO but with wind speed smaller than that in summer. Therefore, although the climatological southeasterly also suppresses type-1 initial errors-induced anomalous northwesterly wind in this season, the loss of latent heat flux induced by the type-1 errors is less decreased (see Figure 11) and then the growth of positive SST errors in the tropical east IO is much smaller than that in summer. During winter and autumn, the climatological mean state presents westerly wind while the type-1 errors still induce anomalous northwesterly wind in the east IO. This

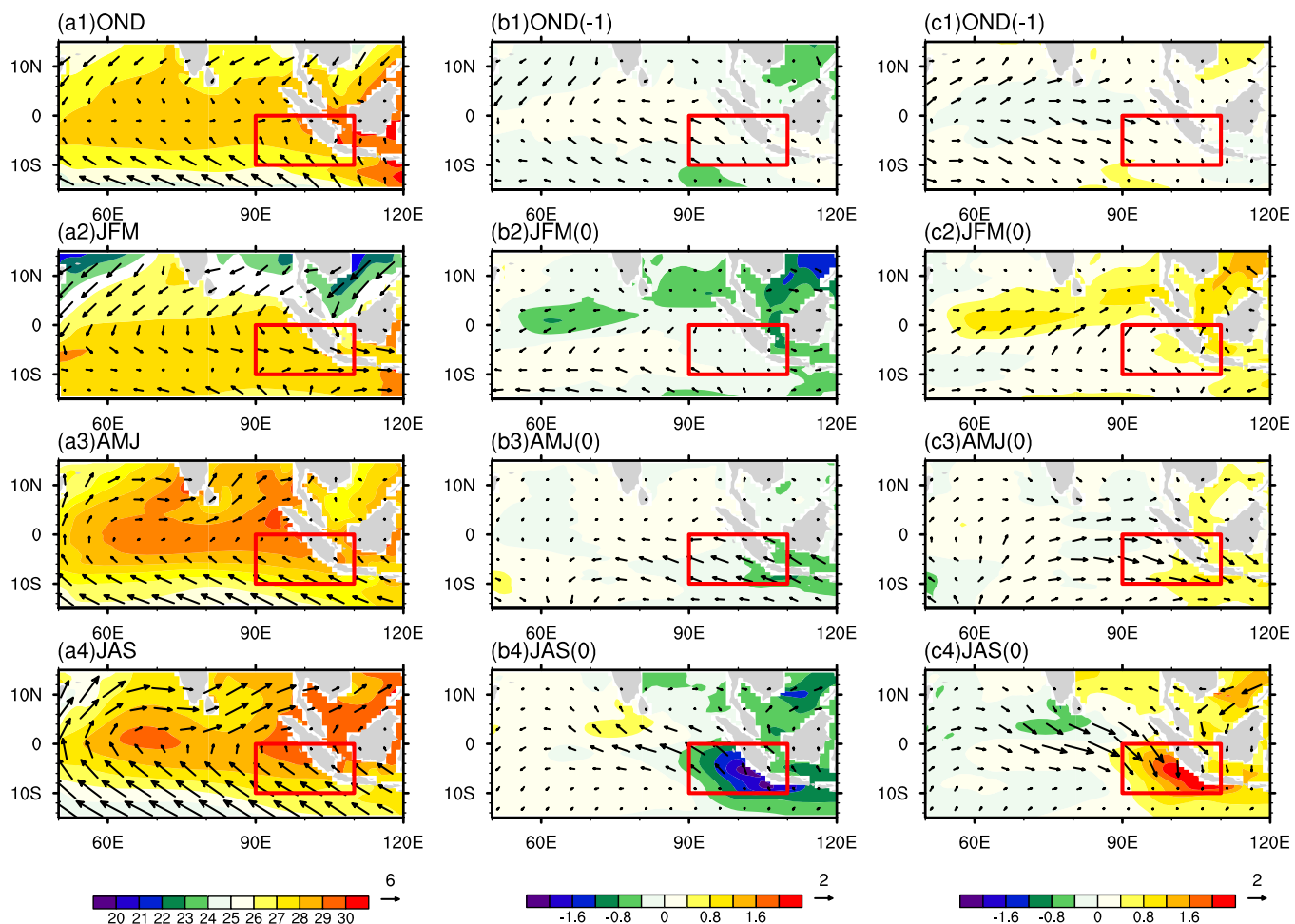


Figure 9. (a) Seasonal mean of climatological SSTs (shaded; units: °C) over the Indian Ocean and its related surface wind (vectors; units: m/s), which are derived by the 150 year integration of the model (see section 2); (b) composites of seasonal SSTAs for the five IOD events and the corresponding surface wind; (c) composites of seasonal SSTs (shaded; units: °C) and surface wind components of the prediction errors with the start month of October (−1) caused by the type-1 initial errors. The red rectangle in the figures denotes the location of the east pole of the IOD.

climatological westerly wind promotes anomalous northwesterly wind of the type-1 errors and increases the loss of latent heat flux, creating negative values for latent heat flux (see Figure 11), which, according to the equation (6), do not favor the growth of positive SST errors during winter and autumn. As such, latent heat flux, due to the effect of the climatological mean state, exhibits the least amount of loss and is of the largest positive value in summer (see Figure 11), which is therefore most favorable for positive SST errors over the east pole growing faster in summer and finally causes a significant SPB for IOD. For type-2 errors, their wind anomalies are quite similar to those of the type-1 errors during spring and summer, with the anomalous northwesterlies wind occurring in the east IO. Therefore, much stronger climatological south-easterlies in summer greatly suppress the corresponding anomalous northwesterly wind and induce larger positive values of latent heat flux in summer, finally more enhancing the growth of the positive SST errors over the east pole of the IOD in summer. During winter and autumn, the east pole of the IOD is covered by the anomalous easterlies induced by the type-2 errors, which are suppressed by the climatological westerly during these two seasons. However, the wind speeds of the climatological westerlies are much smaller during autumn and winter than during summer, which then makes the anomalous easterlies of the type-2 errors be weakly suppressed and the loss of latent heat flux less decreased during autumn and winter. Consequently, the latent heat flux in the equation (6) is positive but small in these two seasons (see Figure 11). This causes the growth of positive SST errors in the east pole is much smaller than that in summer. Obviously, these comparisons show that the growth of the positive SST errors in the east pole of IOD is the largest in summer and that the predictability barrier for IOD tends to occur in summer.

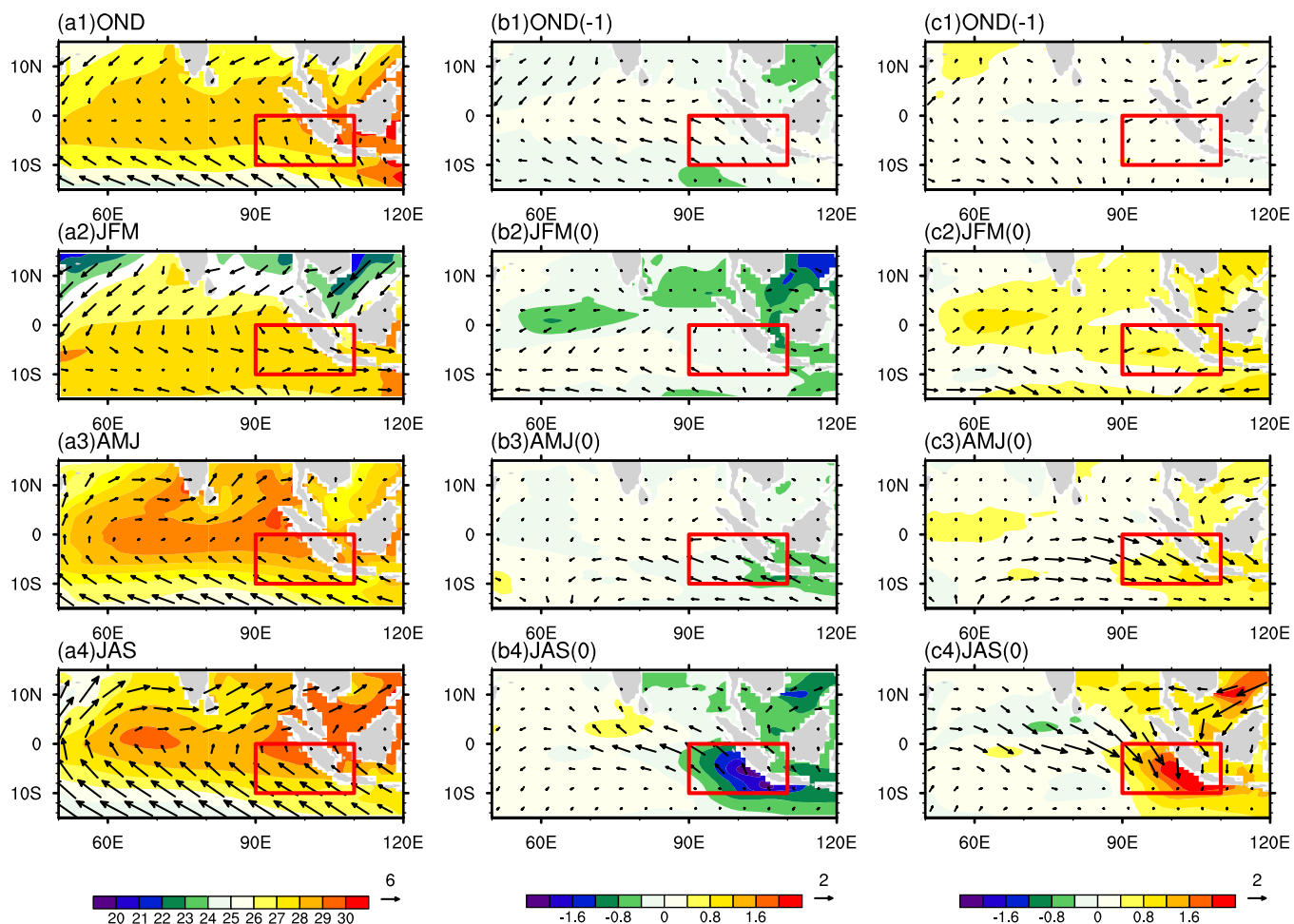


Figure 10. Same as in Figure 9, but for the type-2 initial errors.

From the equation (6), it is shown that, besides the effect of the climatological mean state, the IOD events themselves also play a role in the growth of prediction errors for the IOD, which begs the question as to whether or not they contribute to the SPB for IOD predictions. Since the seasonality of latent heat flux associated with prediction errors for the IOD dominates the SPB, we still focus on latent heat flux to analyze the role of IOD events themselves in the occurrence of the SPB. In fact, winds related to the pIOD events present anomalous southeasterly wind almost in every season but exhibit the strongest anomalous southeasterly wind in summer (see Figures 9 and 10). Such anomalous southeasterly suppress the loss of latent heat flux associated with the prediction errors for the IOD, especially during summer; this causes more positive and larger values of latent heat flux for prediction errors in summer, which finally enhances the growth of the prediction errors for SSTs in the east pole of the IOD and favors the occurrence of the SPB for IOD events.

5. Summary and Discussion

In this paper, the predictability dynamics of Indian Ocean dipole (IOD) events are explored by using the Geophysical Fluid Dynamics Laboratory (GFDL) CM2p1 coupled model from the perspective of error growth. By considering the uncertainties of sea temperature in the Indian Ocean (IO) and Pacific Ocean (PO), it is found that IOD predictions tend to occur the winter predictability barrier (WPB) and the summer predictability barrier (SPB) phenomena. The WPB has been explored in depth in previous studies (Feng & Duan, 2014; Feng et al., 2014a; Luo et al., 2007), and more knowledge is known about its physics. However, the SPB gets less attention, although it was also noticed by Luo et al. (2007), and less is known about it. Previous

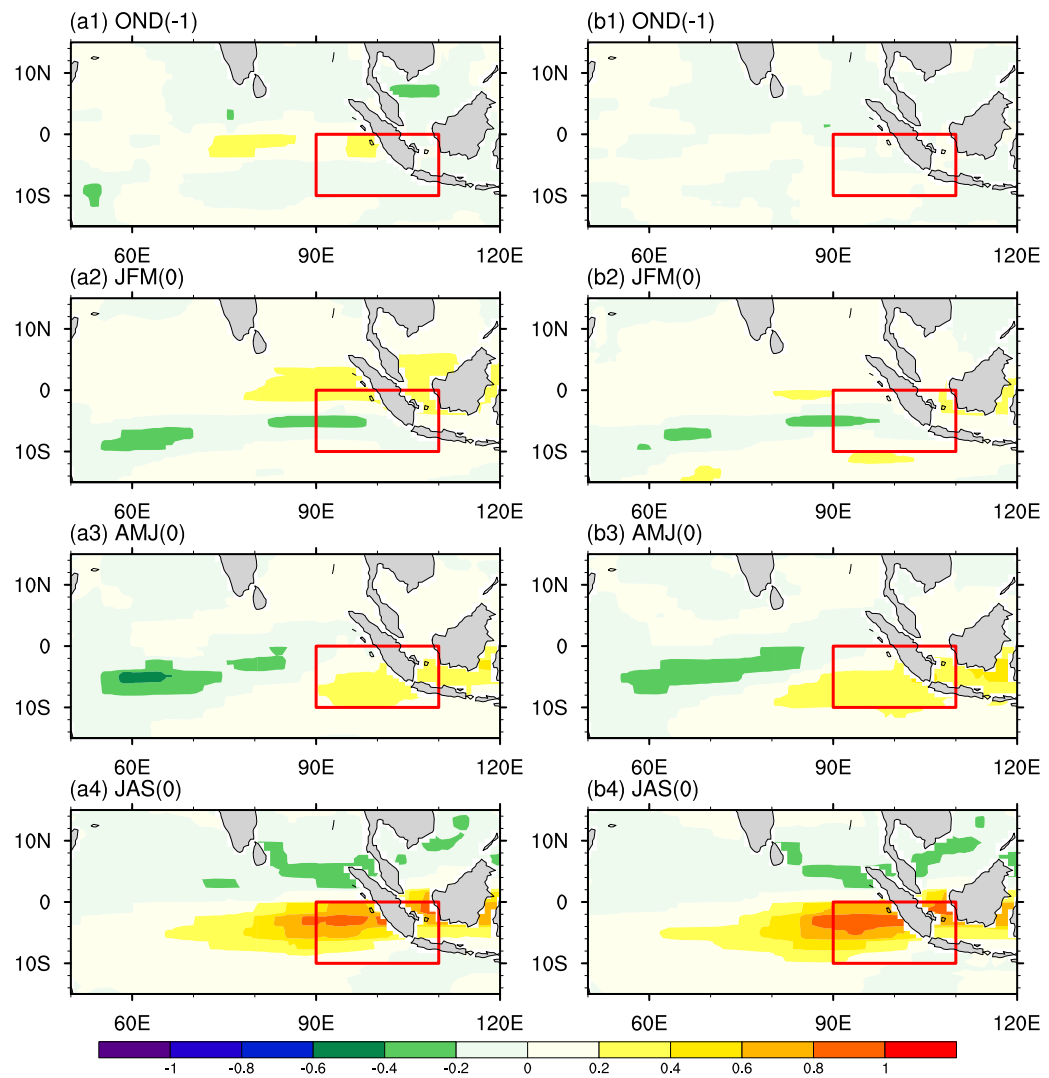


Figure 11. Seasonal mean of latent heat flux errors caused by (a) the type-1 initial errors and (b) the type-2 initial errors for the five IOD events with the start month of October (-1). The positive values indicate the suppression of the loss of the latent heat flux and the negative ones mean the enhancement of the loss of the latent heat flux.

studies demonstrated that the WPB is closely related to initial sea temperature errors in the IO (Feng & Duan, 2014). This study verifies this conclusion and further demonstrates that the SPB can be induced by particular initial sea temperature errors in the Pacific Ocean. Furthermore, features of the initial errors that cause a significant SPB are revealed, and the related two types of initial errors are identified to have significant season-dependent evolutions, with the largest growth occurring in summer. One type of initial error is characterized by large negative sea surface temperature anomalies (SSTAs) in the central-eastern Pacific Ocean, as well as a basin-wide dipole mode in subsurface temperature that has negative anomalies in the upper layers of the eastern equatorial Pacific and positive anomalies in the lower layers of the western equatorial Pacific. The other type almost shows a pattern opposite that of the former type. The large anomalies for both types of initial errors are located in the Pacific Ocean, which also indicates that SPB-related prediction errors mainly result from initial sea temperature errors in the Pacific Ocean.

By tracking the evolution of sea temperature errors induced by the two types of initial errors, it is found that both types of initial errors, despite the nearly opposite spatial structures, exhibit a La Niña-like evolving mode in the Pacific Ocean and a negative IOD evolving mode in the Indian Ocean, with positive SST errors occurring in the east pole ($10^{\circ}\text{S}-0^{\circ}$, $90^{\circ}\text{E}-110^{\circ}\text{E}$) of the IOD. Specifically, the seasonality of positive SST errors in the east pole of the IOD almost dominates the season-dependent evolution of the prediction errors

measured by the dipole mode index (DMI) of the IOD. In addition, a budget analysis shows that the latent heat flux of the prediction errors regulate the seasonality of positive SST errors in the east pole of the IOD. In fact, the type-1 and type-2 error-induced uncertainties in the Pacific Ocean can influence positive SST errors in the east pole of the IOD through the gear effect of the double-cell Walker circulation, suggested by Wu and Meng (1998) and Chen (2011). In fact, the La Niña-like evolving mode in the Pacific Ocean induced by the two types of initial errors favors anomalous easterlies occurring in the PO; correspondingly, anomalous westerlies arising over the Indian Ocean (especially northwesterly in the east pole of the IOD) due to the gear effect of the double-cell Walker circulation. Such anomalous northwesterly wind in the east pole of the IOD are greatly suppressed by strongest climatological southeasterly and reference state IOD event-related anomalous southeasterly during summer. Then, weakened northwesterly winds decrease the loss of latent heat flux associated with the prediction errors, which leads to the latent heat flux term in the equation (6) that exhibits the largest positive value in summer; this is obviously favorable for the fastest growth of positive SST errors over the east pole of the IOD, which then induces the occurrence of the SPB for IOD events.

As mentioned in the introduction, previous studies have shown that IOD predictions often occur the WPB (Feng & Duan, 2014; Feng et al., 2014a; Luo et al., 2007). This study further demonstrates that IOD predictions not only occur the WPB but also the SPB. The occurrence of the predictability barrier negatively influences the prediction skill of IOD events. Specifically, IOD predictions with a 1 year lead time tend to occur prediction barriers that beset two seasons, which may indicate that the IOD has low predictability. In fact, quite a few studies have shown that even though current coupled models reproduce the major features of observed IOD events and adopt advanced initializations to improve initial condition accuracy, the forecast skills of IOD events are still poor (Liu et al., 2014; Luo et al., 2007; Shi et al., 2012; Wajcovicz, 2004). Therefore, the existence of the WPB and SPB for IOD predictions may explain why IOD predictions have a low forecast skill.

The effect of predictability barriers on IOD forecast skill, according to the results shown in this study, can be reduced by improving the initial accuracy. The present study, together with Feng and Duan (2014), emphasized the important role of initial errors in yielding predictability barriers for the IOD. Furthermore, it is noticed that initial sea temperature errors associated with predictability barriers concentrate in few regions (see section 3 and Feng and Duan, 2014). This indicates that the initial errors in these regions contribute to most of the prediction errors for the IOD. That is, the prediction errors for the IOD are most sensitive to the initial errors in these regions and, if increasing additional observations in these regions and assimilating them into the model, the forecast skill of the IOD in summer and winter could be greatly enhanced. This argument is related to the idea of new observational strategy "target observation" (Synder, 1996). Obviously, the results shown here could provide useful information for target observation for IOD predictions. Of course, future work should be done to examine whether or not the regions where initial errors associated with predictability barriers concentrated represent optimal locations for target observations. In addition, it is noticed that the SST errors in the PO sometimes have a much large change from the JFM to AMJ seasons, which may be associated with the famous "spring predictability barrier" phenomenon of Pacific El Niño (Duan et al., 2009; Webster & Yang, 1992). Naturally, it is questioned what the relationship between the summer predictability barrier for IOD and the spring predictability barrier for El Niño is. This is a very interesting question. It is expected that future work can also be done to address this question, which is certainly helpful for understanding the predictability of IOD and then improving the related forecast skill.

Acknowledgments

The authors are very grateful for the useful comments provided by the two anonymous reviewers. This work was jointly sponsored by the National Natural Science Foundation of China (41525017 and 41530961) and the National Program on Global Change and Air-Sea Interaction (GASI-IPOVAL-06). The SODA data used in the present study can be obtained from <http://soda.tamu.edu/data.htm>. The data of land cover, aerosols, tracer gases, and insolation used in the GFDL CM2p1 model can be found at the website <https://www.gfdl.noaa.gov/cm2-5-and-flor/>. The GFDL CM2p1 model data and related codes are stored on the computers at State Key Laboratory of Numerical Modeling for Atmospheric Sciences and Geophysical Fluid Dynamics (LASG; <https://www.lasg.ac.cn>) and will be available to researchers upon request.

References

- Alexander, M. A., Bladé, I., Newman, M., Lanzante, J. R., Lau, N. C., & Scott, J. D. (2002). The atmospheric bridge: The influence of ENSO teleconnections on air-sea interaction over the global oceans. *Journal of Climate*, 15(16), 2205–2231.
- Annamalai, H., & Murtugudde, R. (2004). Role of the Indian Ocean in regional climate variability. *Earth's Climate*, 213–246.
- Ansell, T., Reason, C. J. C., & Meyers, G. (2000). Variability in the tropical southeast Indian Ocean and links with southeast Australian winter rainfall. *Geophysical Research Letters*, 27(24), 3977–3980.
- Ashok, K., Guan, Z., & Yamagata, T. (2001). Impact of the Indian Ocean dipole on the relationship between the Indian monsoon rainfall and ENSO. *Geophysical Research Letters*, 28(23), 4499–4502.
- Ashok, K., Guan, Z., & Yamagata, T. (2003). Influence of the Indian Ocean Dipole on the Australian winter rainfall. *Geophysical Research Letters*, 30(15), 1821. <https://doi.org/10.1029/2003GL017926>
- Birkett, C., Murtugudde, R., & Allan, T. (1999). Indian Ocean climate event brings floods to East Africa's lakes and the Sudd Marsh. *Geophysical Research Letters*, 26(8), 1031–1034.

- Bjerknes, J. (1969). Atmospheric teleconnections from the equatorial Pacific. *Monthly Weather Review*, 97(3), 163–172.
- Black, E., Slingo, J., & Sperber, K. R. (2003). An observational study of the relationship between excessively strong short rains in coastal East Africa and Indian Ocean SST. *Monthly Weather Review*, 131(1), 74–94.
- Cai, W., Cowan, T., & Sullivan, A. (2009). Recent unprecedented skewness towards positive Indian Ocean Dipole occurrences and its impact on Australian rainfall. *Geophysical Research Letters*, 36, L11705. <https://doi.org/10.1029/2009GL037604>
- Carton, J. A., & Giese, B. S. (2008). A reanalysis of ocean climate using simple ocean data assimilation (SODA). *Monthly Weather Review*, 136, 2999–3017.
- Cayan, D. R. (1992). Latent and sensible heat flux anomalies over the northern oceans: Driving the sea surface temperature. *Journal of Physical Oceanography*, 22(8), 859–881.
- Chen, D. (2011). Indo-Pacific Tripole: An intrinsic mode of tropical climate variability. *Advances in Geosciences*, 24, 1–18.
- Clark, C. O., Webster, P. J., & Cole, J. E. (2003). Interdecadal variability of the relationship between the Indian Ocean zonal mode and East African coastal rainfall anomalies. *Journal of Climate*, 16(3), 548–554.
- Delworth, T. L., Broccoli, A. J., Rosati, A., Stouffer, R. J., Balaji, V., Beesley, J. A., et al. (2006). GFDL's CM2 global coupled climate models. Part I: Formulation and simulation characteristics. *Journal of Climate*, 19(5), 643–674.
- Ding, R., & Li, J. (2012). Influences of ENSO teleconnection on the persistence of sea surface temperature in the tropical Indian Ocean. *Journal of Climate*, 25(23), 8177–8195.
- Duan, W., Liu, X., Zhu, K., & Mu, M. (2009). Exploring the initial errors that cause a significant “spring predictability barrier” for El Niño events. *Journal of Geophysical Research*, 114, C04022. <https://doi.org/10.1029/2008JC004925>
- Feng, R., Duan, W., & Mu, M. (2014a). The “winter predictability barrier” for IOD events and its error growth dynamics: Results from a fully coupled GCM. *Journal of Geophysical Research: Oceans*, 119, 8688–8708. <https://doi.org/10.1002/2014JC010473>
- Feng, R., Mu, M., & Duan, W. (2014b). Study on the “winter persistence barrier” of Indian Ocean dipole events using observation data and CMIP5 model outputs. *Theoretical and Applied Climatology*, 118(3), 523–534.
- Feng, R., & Duan, W. S. (2014). The spatial patterns of initial errors related to the “winter predictability barrier” of the Indian Ocean dipole. *Atmospheric and Oceanic Science Letters*, 7(5), 406–410.
- Griffies, S. M. (2009). *Elements of MOM4p1* (GFDL Ocean Group Tech. Rep. 6, 444 pp.). NOAA/Geophysical Fluid Dynamics Laboratory. Retrieved from <http://www.gfdl.noaa.gov/fms>
- Guan, Z., & Yamagata, T. (2003). The unusual summer of 1994 in East Asia: IOD teleconnections. *Geophysical Research Letters*, 30(10), 1544. <https://doi.org/10.1029/2002GL016831>
- Hong, C. C., Li, T., & Kug, J. S. (2008). Asymmetry of the Indian Ocean dipole. Part I: Observational analysis. *Journal of Climate*, 21(18), 4834–4848.
- Li, T., Wang, B., Chang, C. P., & Zhang, Y. (2003). A theory for the Indian Ocean dipole–zonal mode. *Journal of the Atmospheric Sciences*, 60(17), 2119–2135.
- Liu, L., Xie, S. P., Zheng, X. T., Li, T., Du, Y., Huang, G., et al. (2014). Indian Ocean variability in the CMIP5 multi-model ensemble: The zonal dipole mode. *Climate Dynamics*, 43(5–6), 1715–1730.
- Loschnigg, J., Meehl, G. A., Webster, P. J., Arblaster, J. M., & Compo, G. P. (2003). The Asian monsoon, the tropospheric biennial oscillation, and the Indian Ocean zonal mode in the NCAR CSM. *Journal of Climate*, 16(11), 1617–1642.
- Luo, J. J., Masson, S., Behera, S., & Yamagata, T. (2007). Experimental forecasts of the Indian Ocean dipole using a coupled OAGCM. *Journal of Climate*, 20(10), 2178–2190.
- Milly, P. C. D., & Shmakin, A. B. (2002). Global modeling of land water and energy balances. Part I: The land dynamics (LaD) model. *Journal of Hydrometeorology*, 3(3), 283–299.
- Mu, M. Q., & Li, C. Y. (2002). Indian ocean dipole and its relationship with ENSO mode. *Journal of Meteorological Research*, 16(4), 489–497.
- Murtugudde, R., McCreary, J. P., & Busalacchi, A. J. (2000). Oceanic processes associated with anomalous events in the Indian Ocean with relevance to 1997–1998. *Journal of Geophysical Research*, 105(C2), 3295–3306.
- Philander, S. G. H. (1983). El Niño southern oscillation phenomena. *Nature*, 302(5906), 295–301.
- Philander, S. G. H. (1990). *El Niño, La Niña and the Southern Oscillation*. London, UK: Academic Press.
- Saji, N. H., Goswami, B. N., Vinayachandran, P. N., & Yamagata, T. (1999). A dipole mode in the tropical Indian Ocean. *Nature*, 401(6751), 360–363.
- Saji, N. H., & Yamagata, T. (2003a). Structure of SST and surface wind variability during Indian Ocean dipole mode events: COADS observations. *Journal of Climate*, 16(16), 2735–2751.
- Saji, N. H., & Yamagata, T. (2003b). Possible impacts of Indian Ocean dipole mode events on global climate. *Climate Research*, 25(2), 151–169.
- Shi, L., Hendon, H. H., Alves, O., Luo, J. J., Balmaseda, M., & Anderson, D. (2012). How predictable is the Indian Ocean dipole? *Monthly Weather Review*, 140(12), 3867–3884.
- Song, Q., Vecchi, G. A., & Rosati, A. (2007). Indian Ocean variability in the GFDL coupled climate model. *Journal of Climate*, 20(13), 2895–2916.
- Stuecker, M. F., Timmermann, A., Jin, F. F., Chikamoto, Y., Zhang, W., Wittenberg, A. T., et al. (2017). Revisiting ENSO/Indian Ocean Dipole phase relationships. *Geophysical Research Letters*, 44, 2481–2492. <https://doi.org/10.1002/2016GL072308>
- Synder, C. (1996). Summary of an informal workshop on adaptive observations and FASTEX. *Bulletin of the American Meteorological Society*, 77, 953–961.
- Wajswolowicz, R. C. (2004). Climate variability over the tropical Indian Ocean sector in the NSIPP seasonal forecast system. *Journal of Climate*, 17(24), 4783–4804.
- Wajswolowicz, R. C. (2005). Potential predictability of tropical Indian Ocean SST anomalies. *Geophysical Research Letters*, 32, L24702. <https://doi.org/10.1029/2005GL024169>
- Wajswolowicz, R. C. (2007). Seasonal-to-interannual forecasting of tropical Indian Ocean sea surface temperature anomalies: Potential predictability and barriers. *Journal of Climate*, 20(13), 3320–3343.
- Wang, X., & Wang, C. (2014). Different impacts of various El Niño events on the Indian Ocean Dipole. *Climate Dynamics*, 42(3–4), 991–1005.
- Webster, P. J., Moore, A. M., Loschnigg, J. P., & Leben, R. R. (1999). Coupled ocean–atmosphere dynamics in the Indian Ocean during 1997–98. *Nature*, 401(6751), 356–360.
- Webster, P. J., & Yang, S. (1992). Monsoon and ENSO: Selectively interactive systems. *Quarterly Journal of the Royal Meteorological Society*, 118(507), 877–926.
- Wu, G. X., & Meng, W. (1998). Gearing between the Indo-monsoon Circulation and the Pacific–Walker Circulation and the ENSO. Part I: Data Analyses. *Scientia Atmospherica Sinica*, 22, 470–480.
- Yu, J. Y., & Lau, K. M. (2005). Contrasting Indian Ocean SST variability with and without ENSO influence: A coupled atmosphere–ocean GCM study. *Meteorology and Atmospheric Physics*, 90(3), 179–191.
- Zhang, W., Wang, Y., Jin, F. F., Stuecker, M. F., & Turner, A. G. (2015). Impact of different El Niño types on the El Niño/IOD relationship. *Geophysical Research Letters*, 42, 8570–8576. <https://doi.org/10.1002/2015GL065703>